2-1-2011

Medium Propagation Effects in High-Order Harmonic Generation of Ar and N_2

Cheng Jin

Anh-Thu Le
Missouri University of Science and Technology, lea@mst.edu

C. D. Lin

Recommended Citation

C. Jin et al., "Medium Propagation Effects in High-Order Harmonic Generation of Ar and N_2," *Physical Review A - Atomic, Molecular, and Optical Physics*, vol. 83, no. 2, American Physical Society (APS), Feb 2011.
The definitive version is available at https://doi.org/10.1103/PhysRevA.83.023411

Medium propagation effects in high-order harmonic generation of Ar and N_2

Cheng Jin, Anh-Thu Le, and C. D. Lin

J. R. Macdonald Laboratory, Physics Department, Kansas State University, Manhattan, Kansas 66506-2604, USA

(Received 10 December 2010; published 14 February 2011)

We report theoretical calculations of high-order harmonic generation (HHG) by intense infrared lasers in atomic and molecular targets taking into account the macroscopic propagation of both fundamental and harmonic fields. On the examples of Ar and N_2, we demonstrate that these *ab initio* calculations are capable of accurately reproducing available experimental results with isotropic and aligned target media. We further present detailed analysis of HHG intensity and phase under various experimental conditions, in particular, as the wavelength of the driving laser changes. Most importantly, our results strongly support the factorization of HHG at the macroscopic level into a product of a returning electron wave packet and the photorecombination transition dipole under typical experimental conditions. This implies that the single-atom or single-molecule structure information can be retrieved from experimentally measured HHG spectra.

DOI: 10.1103/PhysRevA.83.023411 PACS number(s): 33.80.Rv, 42.65.Ky, 31.70.Hq, 33.80.Eh

I. INTRODUCTION

High-order harmonic generation (HHG) is an extreme nonlinear optical process in which an intense ultrafast infrared light is efficiently converted to an ultrafast coherent extreme ultraviolet (xuv) or soft x-ray light. In the last two decades, HHG has been widely studied for its potential as a short-wavelength light source, either in the form of a useful bright, coherent tabletop light down to the water-window region (280–540 eV) [1,2], or for the production of ultrashort light pulses such as single attosecond pulses and attosecond pulse trains [3,4]. Recently, HHG itself has also been shown to have the potential to image molecular structure with sub-angstrom precision in space and sub-femtosecond precision in time [5–8]. The basic principle of harmonic emission in a gas medium is well understood qualitatively. When an atom or molecule is exposed to an intense laser field, first, at a certain time an electron wave packet tunnels through the barrier formed by the combined atomic and laser fields. Next, it propagates in the laser field and may be driven back to recollide with the target ion. High harmonics are generated when the returning electrons recombine with the ion and convert the energy gained in the laser field to high-energy photons [9,10]. Since the laser field interacts with a macroscopic medium, and the harmonics from all atoms or molecules are generated coherently, a full description of the experimentally observed HHG spectra requires the treatment of the nonlinear propagation of the fundamental laser beam together with the harmonics in the medium. Thus, the study of HHG consists of two parts. The first one is the calculation of the induced dipole by each atom or molecule in the laser field. This is to be carried out quantum mechanically by solving the time-dependent Schrödinger equation (TDSE) or equivalents accurately. The second one is the solving of the nonlinear propagation of the fundamental laser pulse and the harmonic fields in the medium by using Maxwell's equations. As in all nonlinear processes, an efficient harmonic generation requires good phase matching from all the elementary induced dipoles, which in turn depends on a laser's properties such as intensity, pulse duration, pulse shape, and target properties such as gas pressure and position of the gas jet with respect to the laser focus, in addition to the linear and nonlinear responses of gas in the light fields. Clearly, a full understanding of HHG cannot be reached until all of these effects are properly described theoretically. This is especially important if one is to use HHG to image the structure of molecules. Since HHG spectra are sensitive to the detailed experimental conditions which usually cannot be accurately determined in a given experiment, deciding how to extract useful quantitative structure information of individual target molecules in the gas medium is clearly a challenge.

The most accurate way to obtain the induced dipole of an atom or molecule in a laser field is to solve the TDSE numerically. Since this approach is quite time consuming and the calculations have to be carried out for hundreds of laser peak intensities in order to describe the nonuniform laser distributions inside a focused laser beam, this is rarely done in existing studies including macroscopic propagation effect of HHG [11]. Instead, the much simpler strong-field approximation (SFA), or the so-called Lewenstein model [12], is often used to calculate the single-atom response. Despite of this limitation, the temporal and spatial properties of HHG observed experimentally have been reasonably understood from such SFA-based calculations. On the other hand, in a few examples, macroscopic HHG spectra obtained using TSDE-calculated induced dipoles do show significant quantitative discrepancy compared to SFA-based calculations [13,14], and such studies have been limited to a few atomic gases only. To image the structure of molecules from the experimental HHG spectra, one first needs to be able to describe HHG spectra from molecules including macroscopic effects.

In this article, we demonstrate an accurate and efficient method for calculating the HHG spectra from a macroscopic atomic or molecular gaseous medium. The method is based on our recently developed quantitative rescattering (QRS) theory [15–17], which allows us to calculate the induced dipole of an atom or molecule in a laser field with accuracy comparable to those obtained from solving TDSE, yet with computing time comparable to those by using the SFA. More importantly, according to QRS, one can express the complex induced dipole moment as the product of a complex returning wave packet and a complex photorecombination (PR) transition dipole moment, where the former depends on the properties of the laser and the

latter is solely the property of the target. In fact, the elementary PR transition dipole moment is identical to the laser-free elementary photoionization (PI) transition dipole moment which has been well studied in the last few decades. Using the QRS, we further show that the complex returning wave packet can be obtained from the SFA. The validity of the QRS, at the single-atom or single-molecule level, has been carefully calibrated against TDSE results for one-electron model atoms and against experimental HHG spectra from molecules [15]. Clearly such comparison is incomplete without considering the macroscopic propagation effects. In an earlier paper, based on the laser-induced dipoles calculated using the QRS, Jin *et al.* [18] studied the macroscopic propagation effects of the HHG of rare gases theoretically for the situation where the laser intensity and the gas pressure are small. Under this limit, the fundamental laser field is assumed not modified during the propagation. It was shown that the macroscopic HHG spectra after propagation can be expressed as the product of a "macroscopic wave packet" and the same single-atom PR transition dipole. This result is very important since it enables us to extract target structure from the experimentally measured HHG spectra, thus paving the way for using infrared lasers for time-resolved imaging of transient molecules. In the present article, we extend the work of Jin *et al.* [18] to higher laser intensities and gas pressures at which the nonlinear propagation of the fundamental field is considered. We then examine the theoretically simulated HHG spectra of Ar and compare them directly with experimental data. We further extend the method to include molecular targets, which are aligned or isotropically distributed.

In Sec. II, we summarize the method and the essential equations for describing the macroscopic propagation and the calculation of single-atom or single-molecule induced dipoles in the QRS model. We also stress that the HHG spectra should be calculated for each specific experimental condition. Within the QRS, we can define a "macroscopic wave packet" (MWP) which will reflect the effect of lasers and the consequence of propagation in the medium. In Sec. III, the results are shown and analyzed. First, we consider HHG spectra of Ar generated by 1200-nm lasers, and show that the experimental HHG spectra from 30 to 90 eV can be accurately reproduced theoretically based on the QRS, but not on the commonly used SFA. In fact, the HHG spectra depend on the position where and how the xuv light is measured. We show how the two-dimensional HHG spectra, their global behavior, and individual single harmonics in the far field depend on the gas pressure and the pulse length. We also study the spatial distributions of individual harmonics in the near field and in the far field. The phase and the amplitude of the harmonics after propagation are also analyzed for harmonics along the propagation axis and off the axis. The harmonics are found to be always varied with these parameters and the different experimental conditions. However, we find that all the differences can be attributed to the different MWPs. Thus, the dependence of MWP on the gas-jet position with respect to the laser focus, the degree of phase matching with respect to the gas pressure for individual harmonics are investigated. Since the phase-matching condition is also dependent on the wavelength of the laser used, we investigate how macroscopic HHG scales with the laser wavelength. The QRS has been used to obtain induced dipoles from molecules, so we extend the present work to molecular targets. We consider the isotropic and partially aligned molecules and demonstrate that the experimental HHG spectra of N_2 molecules from recent measurements and the present calculations are in good agreement. In Sec. IV, we summarize and discuss future perspective before concluding this paper.

II. THEORETICAL METHOD

A. Propagation of the fundamental field

In an ionizing gas, the propagation of a fundamental driving laser is affected by refraction, nonlinear self-focusing, ionization, and plasma defocusing. The pulse evolution in such a medium is described by a three-dimensional (3D) Maxwell's wave equation [19–21]:

$$\nabla^2 E_1(r,z,t) - \frac{1}{c^2}\frac{\partial^2 E_1(r,z,t)}{\partial t^2} = \mu_0 \frac{\partial J_{\rm abs}(r,z,t)}{\partial t} + \frac{\omega_0^2}{c^2}\left(1-\eta_{\rm eff}^2\right)E_1(r,z,t), \tag{1}$$

where $E_1(r,z,t)$ is the transverse electric field of the fundamental laser pulse with frequency ω_0. In cylindrical coordinates, $\nabla^2 = \nabla_\perp^2 + \partial^2/\partial z^2$, where z is the axial propagation direction. The effective refractive index of the gas medium can be written as

$$\eta_{\rm eff}(r,z,t) = \eta_0(r,z,t) + \eta_2 I(r,z,t) - \frac{\omega_{\rm p}^2(r,z,t)}{2\omega_0^2}. \tag{2}$$

The first term $\eta_0 = 1 + \delta_1 - i\beta_1$ takes into account refraction (δ_1) and absorption (β_1) effects of the neutral atoms, the second term accounts for the optical Kerr nonlinearity which depends on laser intensity $I(t)$, and the third term is from free electrons which contains the plasma frequency $\omega_{\rm p} = [e^2 n_{\rm e}(t)/(\varepsilon_0 m_{\rm e})]^{1/2}$, where $m_{\rm e}$ and e are the mass and charge of an electron, respectively, and $n_{\rm e}(t)$ is the density of free electrons. The absorption term $J_{\rm abs}(t)$ due to the ionization of the medium is expressed as [14,22]

$$J_{\rm abs}(t) = \frac{\gamma(t) n_{\rm e}(t) I_{\rm p} E_1(t)}{|E_1(t)|^2}, \tag{3}$$

where $\gamma(t)$ is the ionization rate, and $I_{\rm p}$ is the ionization potential. This term is usually small under the conditions for harmonic generation [14,22].

The absorption effect (β_1) on the fundamental laser field caused by neutral atoms is in general small, so it is neglected. We only keep the real terms in the refractive index $\eta_{\rm eff}$, and Eq. (1) can be written as

$$\nabla^2 E_1(r,z,t) - \frac{1}{c^2}\frac{\partial^2 E_1(r,z,t)}{\partial t^2} = \mu_0 \frac{\partial J_{\rm abs}(r,z,t)}{\partial t} + \frac{\omega_{\rm p}^2}{c^2}E_1(r,z,t) - 2\frac{\omega_0^2}{c^2}(\delta_1 + \eta_2 I)E_1(r,z,t). \tag{4}$$

By going to a moving coordinate frame ($z' = z$ and $t' = t - z/c$) and neglecting $\partial^2 E_1/\partial z'^2$ since the z' dependence of the electric field is very slow, we obtain [23]

$$\nabla_\perp^2 E_1(r,z',t') - \frac{2}{c}\frac{\partial^2 E_1(r,z',t')}{\partial z'\partial t'} = \mu_0 \frac{\partial J_{\rm abs}(r,z',t')}{\partial t'} + \frac{\omega_{\rm p}^2}{c^2} E_1(r,z',t') - 2\frac{\omega_0^2}{c^2}(\delta_1 + \eta_2 I)E_1(r,z',t'). \quad (5)$$

The temporal derivative in Eq. (5) can be eliminated by a Fourier transform, yielding the equation

$$\nabla_\perp^2 \tilde{E}_1(r,z',\omega) - \frac{2i\omega}{c}\frac{\partial \tilde{E}_1(r,z',\omega)}{\partial z'} = \tilde{G}(r,z',\omega), \quad (6)$$

where

$$\tilde{E}_1(r,z',\omega) = \hat{F}[E_1(r,z',t')], \quad (7)$$

and

$$\tilde{G}(r,z',\omega) = \hat{F}\left\{\mu_0 \frac{\partial J_{\rm abs}(r,z',t')}{\partial t'} + \frac{\omega_{\rm p}^2}{c^2} E_1(r,z',t') - 2\frac{\omega_0^2}{c^2}[\delta_1 + \eta_2 I(r,z',t')]E_1(r,z',t')\right\}, \quad (8)$$

where $\hat{F}$ is the Fourier transform operator acting on the temporal coordinate.

The plasma frequency $\omega_{\rm p}(r,z',t')$ is determined by the free-electron density $n_{\rm e}(t')$, and $n_{\rm e}(t')$ can be calculated as following

$$n_{\rm e}(r,z',t') = n_0\left\{1 - \exp\left[-\int_{-\infty}^{t'} \gamma(r,z',\tau)d\tau\right]\right\}, \quad (9)$$

where n_0 is the neutral atom density, and $\gamma(r,z',\tau)$ is the ionization rate calculated from Ammosov-Delone-Krainov (ADK) theory [24–26]. The refraction coefficient δ_1, depending on the pressure and temperature of the gas medium, is obtained from the Sellmeier equation [27,28]. The second-order refractive index η_2, also depending on pressure of the gas medium, can be calculated through third-order susceptibility $\chi^{(3)}$, which can be measured from experiments [29,30]. Note that the relationship between η_2 and $\chi^{(3)}$ in Koga *et al.* [31] differs from that in Boyd [32] since the latter is derived by using time-averaged intensity of the optical field. The fundamental laser field is assumed to be Gaussian both in space and in time at the entrance of a gas jet ($z' = z_{\rm in}$), and the pressure is assumed constant within the gas jet.

B. Propagation of the harmonic field

The 3D propagation equation of the harmonic field is described by [14,23,33]

$$\nabla^2 E_{\rm h}(r,z,t) - \frac{1}{c^2}\frac{\partial^2 E_{\rm h}(r,z,t)}{\partial t^2} = \mu_0 \frac{\partial^2 P(r,z,t)}{\partial t^2}, \quad (10)$$

where $P(r,z,t)$ is the polarization depending upon the applied optical field $E_1(r,z,t)$. In this equation, the free-electron dispersion is neglected because the frequencies of high harmonics are much higher than the plasma frequency. Again going to a moving coordinate frame and neglecting $\partial^2 E_{\rm h}/\partial z'^2$, Eq. (10) becomes

$$\nabla_\perp^2 E_{\rm h}(r,z',t') - \frac{2}{c}\frac{\partial^2 E_{\rm h}(r,z',t')}{\partial z'\partial t'} = \mu_0 \frac{\partial^2 P(r,z',t')}{\partial t'^2}. \quad (11)$$

We eliminate the temporal derivative by a Fourier transform, obtaining the equation

$$\nabla_\perp^2 \tilde{E}_{\rm h}(r,z',\omega) - \frac{2i\omega}{c}\frac{\partial \tilde{E}_{\rm h}(r,z',\omega)}{\partial z'} = -\omega^2\mu_0 \tilde{P}(r,z',\omega), \quad (12)$$

where

$$\tilde{E}_{\rm h}(r,z',\omega) = \hat{F}[E_{\rm h}(r,z',t')], \quad (13)$$

and

$$\tilde{P}(r,z',\omega) = \hat{F}[P(r,z',t')]. \quad (14)$$

The source term on the right-hand side of Eq. (12) describes the response of the medium to the laser field and includes both linear and nonlinear terms. It is convenient to separate the polarization field into linear and nonlinear components $\tilde{P}(r,z',\omega) = \chi^{(1)}(\omega)\tilde{E}_{\rm h}(r,z',\omega) + \tilde{P}_{\rm nl}(r,z',\omega)$, where the linear susceptibility $\chi^{(1)}(\omega)$ includes both linear dispersion and absorption through its real and imaginary parts, respectively. The nonlinear polarization term $\tilde{P}_{\rm nl}(r,z',\omega)$ can be expressed as

$$\tilde{P}_{\rm nl}(r,z',\omega) = \hat{F}\{[n_0 - n_{\rm e}(r,z',t')]D(r,z',t')\}, \quad (15)$$

where $n_{\rm e}(r,z',t')$ is calculated from Eq. (9) and $D(r,z',t')$ is the single-atom induced dipole moment caused by the fundamental driving laser field.

The refractive index $n(\omega) = \sqrt{1 + \chi^{(1)}(\omega)/\varepsilon_0}$ [32] is related to atomic scattering factors by

$$n(\omega) = 1 - \delta_{\rm h}(\omega) - i\beta_{\rm h}(\omega) = 1 - \frac{1}{2\pi} n_0 r_0 \lambda^2 (f_1 + i f_2), \quad (16)$$

where r_0 is the classical electron radius, λ is the wavelength, n_0 is again the neutral atom density, and f_1 and f_2 are atomic scattering factors which can be obtained from Refs. [34,35]. Note that $\delta_{\rm h}(\omega)$ and $\beta_{\rm h}(\omega)$ account for the dispersion and absorption of the medium on the harmonics, respectively. Finally Eq. (12) can be written as

$$\nabla_\perp^2 \tilde{E}_{\rm h}(r,z',\omega) - \frac{2i\omega}{c}\frac{\partial \tilde{E}_{\rm h}(r,z',\omega)}{\partial z'} - \frac{2\omega^2}{c^2}(\delta_{\rm h} + i\beta_{\rm h})\tilde{E}_{\rm h}(r,z',\omega) = -\omega^2\mu_0 \tilde{P}_{\rm nl}(r,z',\omega), \quad (17)$$

where the nonlinear polarization as the source of the harmonics is explicitly given. After the propagation in the medium, we obtain the near-field harmonics at the exit face of the gas jet ($z' = z_{\rm out}$).

As presented in Ref. [18], when both the pressure and the laser intensity are low, the fundamental field is not modified through the medium. In other words, the source term in Eq. (1) can be taken as zero. Then the fundamental laser field, assuming to be a Gaussian beam spatially, is given approximately in an analytical form. For the harmonic field, the dispersion and absorption effects from the medium, which are explicitly expressed as a dispersion-absorption term in

Eq. (17), are not included. These effects would become important if the gas pressure is high. For molecular targets, we will limit ourselves to experiments carried out under the conditions of low laser intensity and low gas pressure. Note that Eqs. (6) and (17) are solved using a Crank-Nicholson routine for each value of ω. Typical parameters used in the calculations are 200–300 grid points along the radial direction and 400 grid points along the longitudinal direction.

C. Far-field harmonic emission

Experimentally, harmonics are not measured at the exit face of a gas medium. They may go through a slit, an iris, or a pinhole or be reflected by a mirror before they reach the detector. The far-field harmonic emissions can be obtained from near-field harmonic emissions at the exit face of a gas medium through a Hankel transformation [36–38],

$$E_{\rm h}^{\rm f}(r_{\rm f},z_{\rm f},\omega) = -ik\int \frac{\tilde{E}_{\rm h}(r,z',\omega)}{z_{\rm f}-z'} J_0\left(\frac{krr_{\rm f}}{z_{\rm f}-z'}\right) \times \exp\left[\frac{ik(r^2+r_{\rm f}^2)}{2(z_{\rm f}-z')}\right] rdr, \quad (18)$$

where J_0 is the zero-order Bessel function, $z_{\rm f}$ is the far-field position from the laser focus, $r_{\rm f}$ is the transverse coordinate in the far field, and the wave vector k is given by $k = \omega/c$.

Suppose the harmonics in the far field are collected from an extended area; the power spectrum of the macroscopic harmonics is obtained by integrating harmonic yields over the area:

$$S_{\rm h}(\omega) \propto \iint \left|E_{\rm h}^{\rm f}(x_{\rm f},y_{\rm f},z_{\rm f},\omega)\right|^2 dx_{\rm f}dy_{\rm f}, \quad (19)$$

where $x_{\rm f}$ and $y_{\rm f}$ are the Cartesian coordinates on the plane perpendicular to the propagation direction, and $r_{\rm f} = \sqrt{x_{\rm f}^2+y_{\rm f}^2}$.

D. Quantitative rescattering theory

In this work, the single-atom (or single-molecule) induced dipole moment $D(t')$ in Eq. (15) is calculated quantum mechanically using the QRS theory. A detailed discussion of QRS for HHG from atoms or molecules is given in Ref. [17]. We briefly discuss the QRS theory for atoms and molecules separately in the following.

1. Atomic target

According to the QRS, the induced dipole moment $D(\omega)$ can be written as [39]

$$D(\omega) = W(\omega)d(\omega), \quad (20)$$

where $d(\omega)$ is the complex PR transition dipole matrix element and $W(\omega)$ is the complex microscopic wave packet. $|W(\omega)|^2$ describes the flux of the returning electrons and is the property of the laser only. The QRS is a simple model that improves the SFA. It replaces the plane wave used in the SFA with an accurate scattering wave in the calculation of PR transition dipole matrix elements, while the returning microscopic wave packet is the same as that in the SFA. Since the electron wave packet after tunneling but before the recombination is governed mostly by the laser field while the electron is far away from the target ion, and such interaction is fully described by the SFA, this explains why the electron wave packet (its dependence on the momentum of returning electrons) derived from the SFA is accurate. In practical applications, the QRS obtains the induced dipole moment by

$$D^{\rm QRS}(\omega) = D^{\rm SFA}(\omega)\frac{d^{\rm QRS}(\omega)}{d^{\rm SFA}(\omega)}, \quad (21)$$

where both $D^{\rm SFA}(\omega)$ and $d^{\rm QRS}(\omega)$ are complex numbers, while $d^{\rm SFA}(\omega)$ is either a pure real or pure imaginary number. Within the single active electron (SAE) approximation, we calculate $d^{\rm QRS}(\omega)$ using "exact" numerical wave functions for the bound and continuum states. For Ar, we use the model potential given by Müller [40],

$$V(r) = -[1 + Ae^{-r} + (17-A)e^{-Cr}]/r, \quad (22)$$

with ($A = 5.4$, $C = 3.682$). In this model, spin-orbit interaction is neglected. The parameters have been chosen such that the minimum in the PI (or PR) cross section is reproduced correctly. We comment that in principle the parameters in Eq. (21) can be generalized to many-electron wave functions if needed.

2. Molecular target

Within the QRS theory, the induced dipole moment $D(\omega,\theta)$ for a fixed-in-space molecule is given explicitly by

$$D(\omega,\theta) = N(\theta)^{1/2}W(\omega)d(\omega,\theta), \quad (23)$$

where $N(\theta)$ is the alignment-dependent ionization probability, $W(\omega)$ is the microscopic wave packet, and $d(\omega,\theta)$ is the alignment-dependent transition dipole (complex in general). Here θ is angle between the molecular axis with respect to the laser's polarization. We limit ourselves here to linearly polarized lights and linear molecules and consider the parallel component of HHG with respect to the laser polarization only. Thus, only the parallel component of the transition dipole $d(\omega,\theta)$ is needed in the calculation. Note that $W(\omega)$ does not depend on the alignment angle θ, and it can be calculated formally as

$$W(\omega) = \frac{D(\omega,\theta)}{N(\theta)^{1/2}d(\omega,\theta)}. \quad (24)$$

Recall that $W(\omega)$ can be obtained from SFA, where all the matrix elements above are calculated by replacing the continuum waves with plane waves. Since the wave packet $W(\omega)$ is independent of the alignment angle θ, it needs to be calculated only once for a given angle θ. In the QRS, the single-molecule induced dipole moment by the same laser is then obtained from Eq. (24) by combining with the accurate $d(\omega,\theta)$ obtained from quantum chemistry code [41] and with the tunneling ionization rate $N(\theta)$ obtained from the MO-ADK theory [25,42]. Applications of the QRS for HHG from single molecules have been investigated previously [17,43,44].

Linear molecules can only be partially aligned when they are placed in a short laser field (pump laser) [45]. The intensity of the aligning laser is usually weak and not tightly focused such that it can be assumed to be constant within the gas medium. In other words, the degree of molecular alignment is not varied in the medium. In the following, the polarization of

aligning laser is assumed to be parallel to the probe laser. The averaged induced dipole from the partially aligned molecules at each point in the gas medium is then obtained by coherently averaging induced dipole moments over the molecular angular distributions, that is,

$$D^{\rm avg}(\omega) = \int_0^\pi D(\omega,\theta)\rho(\theta)\sin\theta d\theta, \tag{25}$$

where $\rho(\theta)$ is the angular (or alignment) distribution of the molecules. Similarly, the free electron density in Eq. (15) is replaced by the averaged one:

$$n_{\rm e}^{\rm avg}(t') = \int_0^\pi n_{\rm e}(t',\theta)\rho(\theta)\sin\theta d\theta, \tag{26}$$

where $n_{\rm e}(t',\theta)$ is the alignment-dependent ionization probability derived from Eq. (9). For randomly distributed molecules, $\rho(\theta)$ is a constant. Once the averaged induced dipoles $D^{\rm avg}(\omega)$ are obtained for a number of different laser intensities, they are then fed into the propagation equations for the harmonics. The propagation is then carried out similar to that for atomic targets. We comment that in this model, dielectric properties of molecules due to nonisotropic distributions have been neglected.

E. Macroscopic wave packet

As presented in Ref. [18] [see their Eq. (25)], the macroscopic HHG spectrum in the near field for atomic targets can be expressed as

$$S_{\rm h}(\omega) \propto \omega^4 |W'(\omega)|^2 |d(\omega)|^2, \tag{27}$$

where $W'(\omega)$ is called a MWP, and $d(\omega)$ is the PR transition dipole moment. This relation still holds in the far field [see Eq. (19)], since the PR transition dipole can be factorized out in Eq. (18). The propagation of harmonics in free space to the far field would thus only modify the MWP.

If molecules are only partially aligned, we calculate $d(\omega)$ by coherently averaging the PR transition dipole weighted by the ionization probability of $N(\theta)$ [25,42]:

$$d^{\rm avg}(\omega) = \int_0^\pi N(\theta)^{1/2} d(\omega,\theta)\rho(\theta)\sin\theta d\theta. \tag{28}$$

From Eq. (27), the target structure is reflected in the PR transition dipole; the propagation effect of the harmonics, in the meantime, is incorporated in the MWP. The two properties are well separated. The MWP represents the cumulative effect of the returning electron wave packet (or microscopic wave packet) after propagation in the medium and in the free space. The validity of Eq. (27) forms the basis of extracting target molecular structure information from the experimentally measured HHG spectra.

III. RESULTS AND DISCUSSION

A. Macroscopic HHG spectra of Ar: Theory vs experiment

In Fig. 1, we show the macroscopic HHG spectra generated by a 1200-nm laser. Experimentally [46], a 0.5-mm-long gas jet was placed 3 mm after the laser focus ($z = 3$ mm). A vertical slit with a width of 100 μm is placed 24 cm after the gas jet. The beam waist at the laser focus is 47.5 μm, and the laser pulse duration is ~40 fs. Laser peak intensity in the center of gas jet was 1.6×10^{14} W/cm^2, and the pressure of gas jet was estimated to be 28 Torr. In the simulation, the laser peak intensity and the pressure are adjusted until the best agreement with the experiment is reached visually. Using peak intensity of 1.5×10^{14} W/cm^2, we find the best agreement with the cutoff position in the HHG spectra, and at pressure of 84 Torr, we find the best agreement in the widths of the harmonics [46].

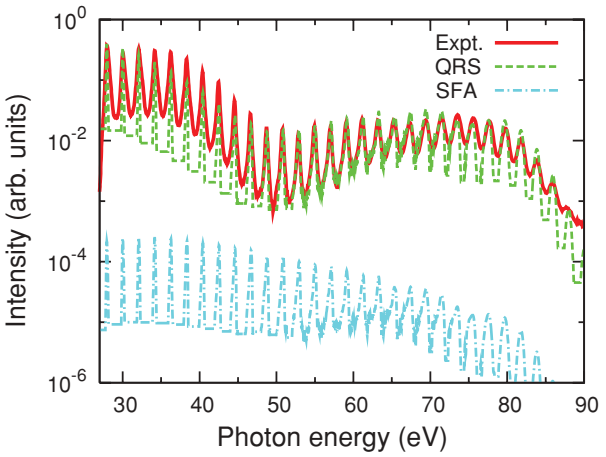

FIG. 1. (Color online) Comparison of theoretical (QRS, dotted line; SFA, dot-dashed line) and experimental (solid line) HHG yields of Ar under a 1200-nm laser. Experimental data are from Ref. [46]. Laser parameters are given in the text.

We first calculate the single-atom response either by QRS or SFA. In SFA, Ar is treated as an effective "hydrogenlike" atom where the nuclear charge is chosen such that its 1s binding energy is the same as the binding energy of Ar. The induced dipole moment is calculated by using the Lewenstein model [12]. In the QRS, the "exact" transition dipole is calculated by using the model potential given by Müller [40]. The single-atom response is then fed into Eq. (17), and the harmonic signals are collected in the far field in terms of Eq. (19).

In Fig. 1, we can see very good agreement between QRS and experiment over the photon-energy region of 30–90 eV. The "famous" Cooper minimum in Ar [47] is clearly seen in both experimental and theoretical spectra. The Cooper minimum in Ar has been reported in early HHG spectra generated by 800-nm lasers [48,49], and it is seen more prominently using long-wavelength lasers [50]. Meanwhile, the propagated spectra obtained from SFA do not show the Cooper minimum, nor does it reproduce the general spectral shape. Note that the Cooper minimum shall occur in the single-atom HHG spectra but it does not always appear in the macroscopic HHG spectra. As illustrated in recent simulations [46], the position of the Cooper minimum can change or even disappear under different experimental conditions. Such conclusions are consistent with experimental data where the Cooper minimum may disappear in the HHG spectra by changing the gas pressure [49] or by changing the gas-jet position with respect to the laser focus [51]. In the following, we show that these changes are due to variations in the MWP, and the separability of Eq. (27) is still valid.

In Fig. 1, there are still small discrepancies between the experimental data and the simulation by QRS despite

various attempts using somewhat different laser parameters. The harmonic width (or harmonic chirp) in the simulation is narrower than that in the experimental data. The harmonic width is mainly determined by laser intensity, pulse duration, and gas pressure [52–54]. In the experiments, parameters such as pressure of the gas jet and laser intensity and its spatial distribution cannot be measured precisely. Other factors, such as the use of the slit and the position of the detector, can also influence the HHG spectra. All of these uncertainties can contribute to the discrepancy between the simulation and the measured HHG spectra. On the other hand, as seen from Fig. 1, the overall agreement between the experiment and the simulation over the 30-to-90-eV region is quite satisfactory.

B. Harmonic chirp

Although Fig. 1 shows the general global agreement between simulation and experimental data, it is pertinent to examine typical individual harmonics more carefully. How does the spectral width (or the harmonic chirp) vary as the pulse duration, gas pressure, and laser intensity are changed? In Fig. 1 the harmonics were taken for the gas jet placed after the laser focus; thus, short trajectories were selected. In this case, the harmonic chirp is less dependent on the laser intensity, especially for a long-wavelength laser [55]. We actually vary the laser intensity by 20%; the harmonic width almost does not change (not shown). We concentrate on the effects of the pulse duration and gas pressure here only.

In Figs. 2(a)–2(c), we show the spatial distribution of harmonic emission in the far field (24 cm after the gas jet) by varying laser duration and gas pressure. All the other parameters are kept the same as in Fig. 1. For each harmonic, the distribution on the vertical plane is shown. Integration of harmonic intensity over the vertical dimension in Fig. 2(b) gives the simulated HHG spectra by QRS in Fig. 1. A longer pulse duration and/or a lower pressure tend to generate sharper (narrower width) lower-order harmonics. A careful

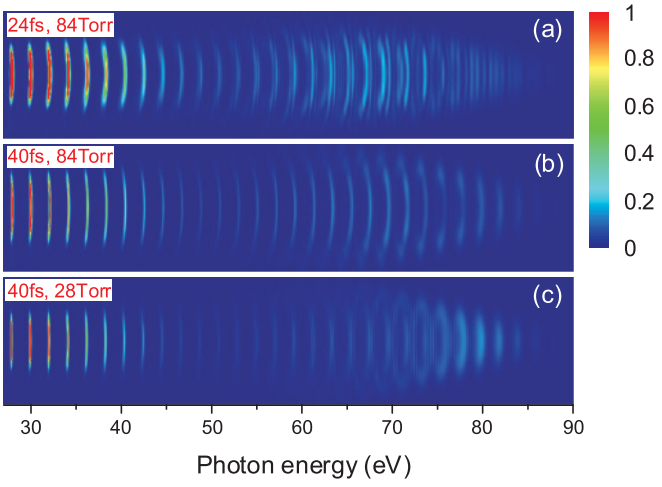

FIG. 2. (Color online) Spatial distributions of harmonic emission vs photon energy (normalized using on-axis intensity at 77 eV) in the far field for the laser with different pulse durations and the gas jet with different pressures: (a) 24 fs, 84 Torr; (b) 40 fs, 84 Torr; and (c) 40 fs, 28 Torr. The other laser parameters are not varied and are given in the text.

inspection reveals that the peak position of the harmonic actually blue-shifted from one frame to another. The shift is due to the change of the fundamental pulse as it propagates through the nonlinear medium [11]. In addition, the higher harmonics are less sharp, reflecting that the quality of phase matching varies with harmonic orders.

In Figs. 3(a)–3(d), we show the spectral distributions of harmonics H27 (27th harmonic), H37, H57, and H77, respectively, after they have been integrated along the vertical dimension. Here we examine the change of harmonic width as the pulse length and/or gas pressure are varied. Recall that the harmonic peaks are blue-shifted differently for different conditions. For easy comparison, the peak position is taken to be from the 40 fs, 84 Torr set (red, solid lines). The spectra from the other two sets are shifted to have the same peak position. From the figures, for H27 and H37, clearly the harmonic width increases with decreasing pulse duration. For a given pulse duration, the width increases with gas pressure. These figures also show that phase matching is not good for the higher harmonics, especially for the short-duration pulses where high-energy photons are emitted only from a few half cycles. For these higher harmonics, narrower width seems to be obtained by raising the gas pressure.

The harmonic chirp is a direct consequence of temporal variation of laser intensity, which can be measured by cross-correlation frequency resolved optical gating [56,57]. It is determined by $\Delta\omega(t) = -\partial\Phi(\omega,t)/\partial t$. The harmonic phase $\Phi(\omega,t)$ is proportional to laser intensity $I(t)$, with larger proportionality constant for electrons taking long trajectories than for short trajectories [58] [see their Eq. (1)]. For the focusing conditions in the present case, only short trajectories are selected and longer pulse leads to narrower harmonic width. In our model, the Kerr effect on the fundamental field and plasma effect due to free electron are included in Eq. (2). The $\Phi(\omega,t)$ is dependent on the gas pressure through η_2 and $n_e(t)$. It can be understood that the only variation of gas pressure could lead to the change of harmonic width. We further comment that stronger plasma defocusing effect caused by increasing the gas pressure might contribute to the observed changes in the harmonic spectral widths. Similar analysis of the dependence of phase-matching on gas pressure can be found in Refs. [59,60].

C. Harmonic divergence

We next examine the harmonic emission in the near field and in the far field. The laser parameters are the same as those in the simulation in Fig. 1. Figures 4(a) and 4(b) show that harmonic emissions in the near field are quite messy spatially [18]. Because the harmonics are generated from a nonuniform Gaussian beam, the phase-matching condition in the medium varies spatially. The radial variation of the phase $\Phi(\omega,r)$ introduces a curvature of the phase front, which makes the harmonic emission divergent [58]. After further propagating to the far field, the harmonic emissions become regular [see Fig. 4(c)], where harmonics display Gaussian distributions centered at the propagation axis. In Fig. 4(c), only the short trajectories are selected. The harmonic emission is mainly on axis because of the small divergence. Since a long-wavelength laser is used [61], the divergence in the region from H35 to H65

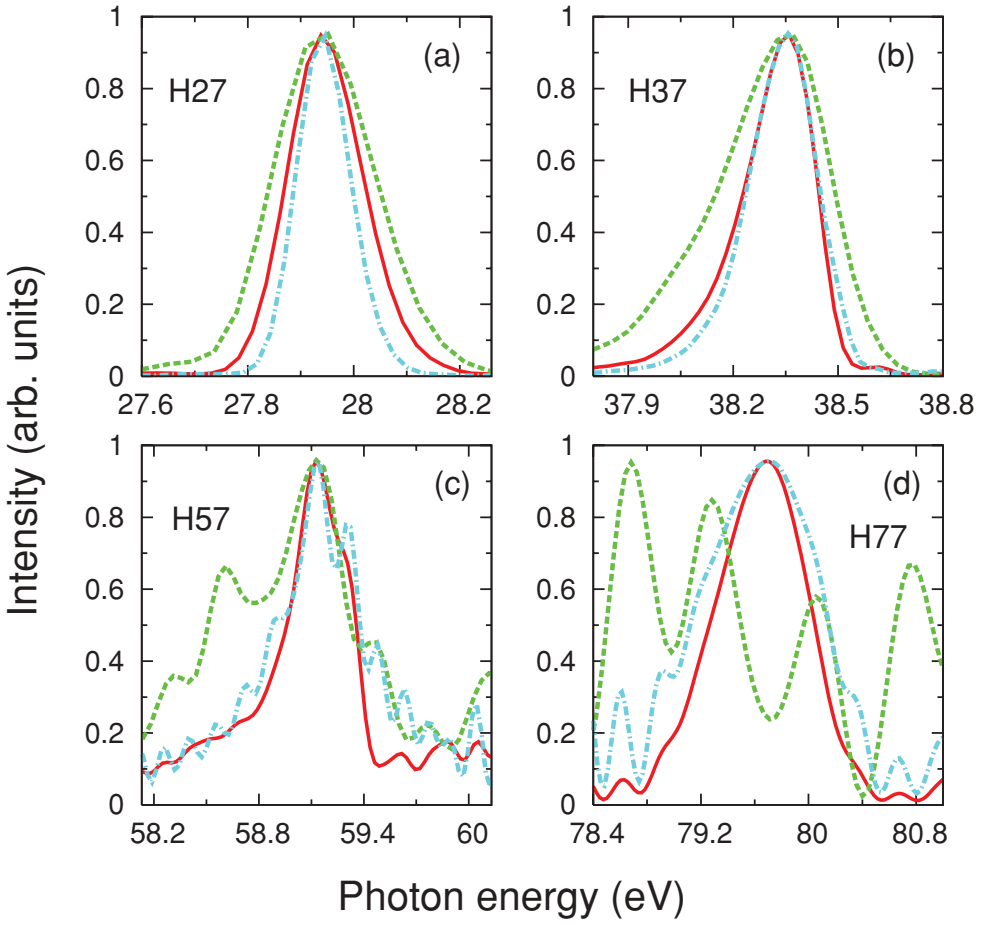

FIG. 3. (Color online) The dependence of spectral distribution of individual harmonics on experimental conditions. The spectra are integrated over the vertical dimension as shown in Fig. 2. Experimental conditions are 40 fs, 84 Torr (red, solid lines); 24 fs, 84 Torr (green, dashed lines); and 40 fs, 28 Torr (blue, dot-dashed lines). Note that the peak position of the harmonic in each frame has been shifted to coincide for easy comparison.

does not change too much. Similar study of the divergence of harmonics has been done for short-wavelength lasers [62].

We also study the phase of harmonics vs the radial distance in Fig. 4(d). For each harmonic, we note that the calculated phase grows quadratically with the radial distance and scales almost linearly with the frequency of the harmonics. The phases near the propagation axis vary for different harmonics [see the inset of Fig. 4(d)]. Below we show that the behaviors of intensity and phase of harmonics in the far field display good (laserlike) spatial Gaussian character.

Recall that an incident Gaussian beam focused at $z = 0$ propagating along the z axis [18,36,37] is given by

$$E(r,z) = \frac{bE_0}{b+2iz}\exp\left(-\frac{kr^2}{b+2iz}\right) = |E(r,z)|e^{i\varphi(r,z)}, \quad (29)$$

where

$$|E(r,z)| = \frac{bE_0}{(b^2+4z^2)^{1/2}}\exp\left(-\frac{kr^2 b}{b^2+4z^2}\right), \quad (30)$$

and

$$\varphi(r,z) = -\tan^{-1}\left(\frac{2z}{b}\right) + \frac{2kr^2 z}{b^2+4z^2}. \quad (31)$$

Here E_0 is the peak field at the focus, k is the wave vector, $b = 2\pi w_0/\lambda$ is the confocal parameter, w_0 is the beam waist at the focus, and λ is the wavelength. The intensity of each harmonic in Fig. 4(c) follows the square of Eq. (30). The phase increases quadratically with r and linearly with the harmonic order, as seen in Fig. 4(d), and can be seen to follow the second term of Eq. (31). Near $r = 0$, the phase from the first term of Eq. (31) also contributes. This term (multiplied by harmonic order) gives a phase between $-\pi$ and π for each harmonic, as seen in the inset of Fig. 4(d), in which the phase at $r = 0$ is only defined within 2π. Since for different harmonics the confocal parameters are probably changed either due to beam waist or wavelength, and the focus position may also change, we can only claim that each harmonic beam after propagation is close to a Gaussian beam qualitatively, but not necessarily quantitatively. A similar study of the phase of the harmonics in the near field was presented in Ref. [63].

D. Harmonic phase vs photon energy in the far field

In the QRS model for single-atom response, the phase of each harmonic is the sum of the phase from the microscopic wave packet and the phase from the transition dipole [see Eq. (20)]. For the harmonics calculated from the SFA, it is

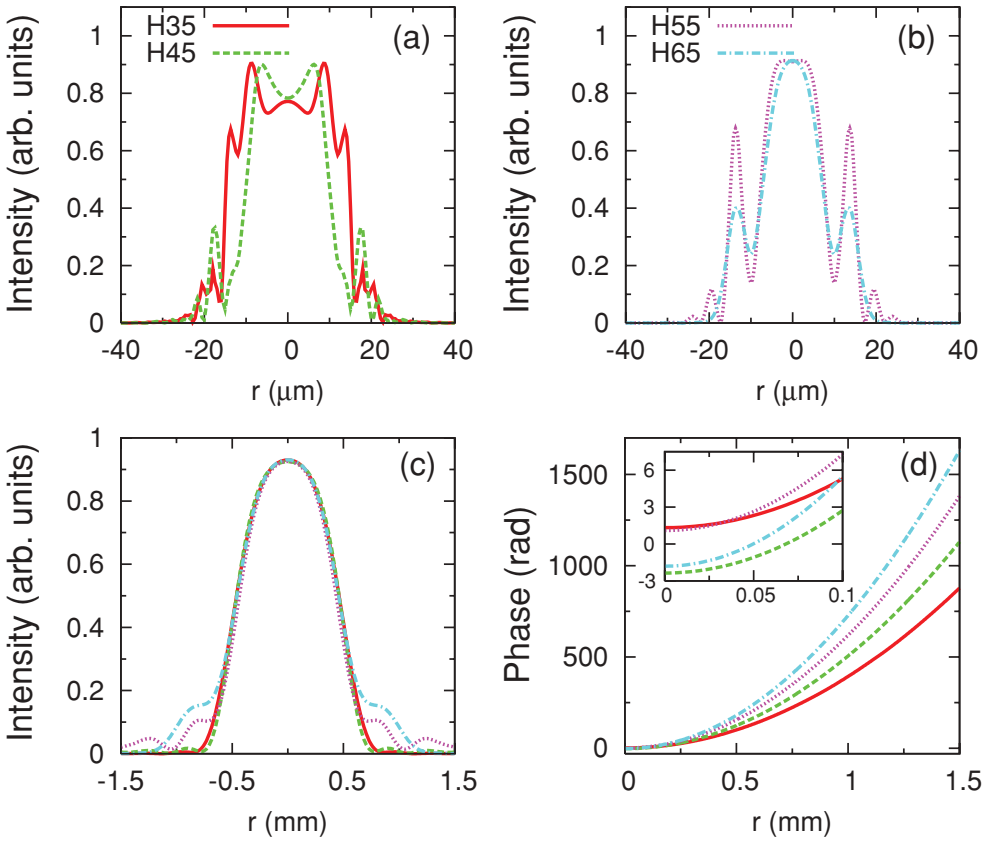

FIG. 4. (Color online) Spatial dependence of harmonic emission in the near field (at the exit of gas jet): (a) H35 and H45, (b) H55 and H65, and in the far field (at the entrance of slit): (c) H35–H65. (d) Spatial dependence of phases for H35–H65 in the far field. Inset: Phases of H35–H65 in the region close to the propagation axis.

the same sum except that the phase of the transition dipole is either 0 or π. Thus, the difference in the harmonic phase calculated from the QRS and from the SFA is given by the phase of the transition dipole calculated within the QRS (modulus π). Is this relation still correct after the propagation, as implied by Eq. (27)? In Figs. 5(a)–5(c), we show phase differences (squares) calculated by QRS and by SFA for far-field harmonics and compare them with the phase $\phi(\omega)$ of the transition dipole from the QRS (solid line) at $r = 0$ mm, 0.5 mm, and 1.5 mm. The laser parameters are the same as those in Fig. 1. The two are in good agreement. This agreement implies that the phase of the MWP $W'(x,y,\omega)$ obtained from QRS and from SFA remains identical after propagation at any points (x,y) on the plane. (In next section we show that the magnitude of the MWP is also the same.)

For the generation of attosecond pulses, the phase difference (or attochirp) between consecutive harmonics is crucial [64]. The above results indicate that attochirp calculated using QRS and SFA differs only by the difference of the phase $\phi(\omega)$ of the transition dipole between two neighboring harmonics. This difference divided by $2\omega_0$ (in units of eV), or the derivative of $\phi(\omega)$ with respect to ω (in units of eV), is shown (dashed line) in Fig. 5(a). It is clear that correction to the attochirp calculated from SFA is small, except in the region near the Cooper minimum where the phase $\phi(\omega)$ changes rapidly. This result is very significant since it explains why the generation of attosecond pulses can be understood mostly based on the SFA theory, even though it does not predict the harmonic spectra accurately. The phase of each harmonic is mostly determined by the phase of the returning electron wave packet, which has been accurately accounted for by the SFA, with very small corrections from the recombination process. This simplification explains why it is possible to study the generation of attosecond pulses in the past decade without a quantitatively accurate theory of HHG.

To appreciate the complexities of harmonics, in Figs. 5(d)–5(f) we show the far-field harmonic emissions at different radial distances r from the propagation axis. The harmonic emissions for different photon energies are comparable close to the axis, to provide a broad energy region from the on-axis area to synthesize attosecond pulses [65]. In the experiment this is accomplished by employing an iris [64]. We note that at $r = 0$ mm and $r = 0.5$ mm, the harmonic spectra resemble each other and the broad Cooper minimum can be easily identified. This is not the case if the spectra are taken at $r = 1.5$ mm, where the signals are much weaker and the Cooper minimum is no longer visible. As mentioned in Sec. III A, the "disappearance" of the Cooper minimum is attributed to the change of MWP, not due to the recombination process. Experimentally the "disappearance" of the Cooper minimum in the HHG spectra of Ar has been shown using 800-nm pulses by changing the experimental conditions [49,51].

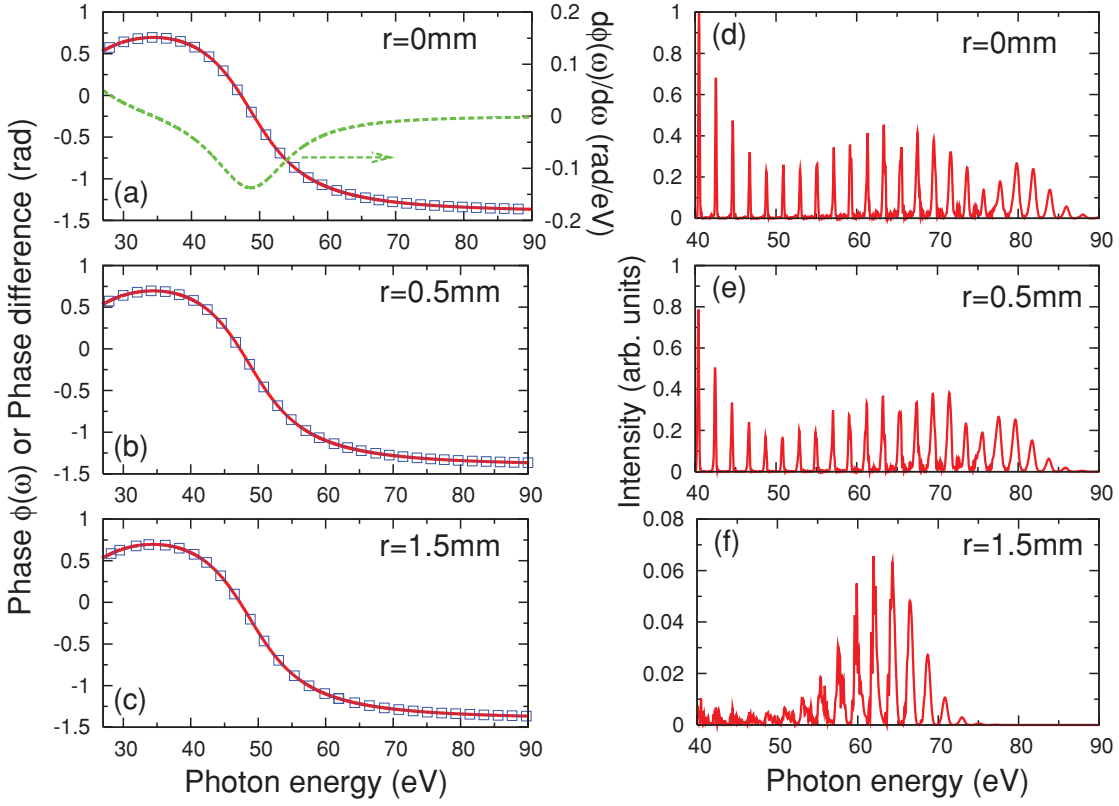

FIG. 5. (Color online) Phase difference (open squares) between far-field harmonics by QRS and by SFA, in comparison with the phase $\phi(\omega)$ (solid lines) of "exact" transition dipole, at (a) $r = 0$ mm, (b) $r = 0.5$ mm, and (c) $r = 1.5$ mm. The difference of attochirp (the phase difference divided by the energy difference between two neighboring harmonics) between the QRS and the SFA is shown in (a) (dashed line). (d)–(f) The far-field harmonic emissions at $r = 0$ mm, $r = 0.5$ mm, and $r = 1.5$ mm, respectively, vs photon energy. Note that the phases in (a)–(c) are only taken at harmonic peaks, which are shown in (d)–(f), respectively.

E. The dependence of MWP on experimental conditions

In Fig. 6(a) we show how the MWP (complex amplitude) changes with the gas-jet position calculated by the QRS for HHG signal collected after the slit. For simplicity, only the envelope of the MWP is plotted. We keep laser intensity at 1.6×10^{14} W/cm^2 and gas pressure at 56 Torr. The slit is placed 24 cm after the gas jet, and all other parameters are the same as given in Fig. 1. We also show the MWP calculated by SFA under exactly the same conditions, and the results are shown (circles) in Fig. 6(a). The comparison shows that the MWPs (magnitude) from QRS and from SFA are the same for the same experimental condition, even though the MWP can change greatly depending on the gas-jet position. When the gas jet is placed "after" the laser focus ($z = 3$ mm) the MWP is very flat, since good phase-matching is favored for this arrangement as the single-atom harmonic phase is partially canceled by the Gouy phase from the focused laser [63,66]. If the gas jet is placed before the laser focus, we note that the MWP changes rapidly, especially near photon energy around 50 eV. Such strong energy dependence can wash out the Cooper minimum in the HHG spectra [46].

In Fig. 6(b) we compare the MWPs as in Fig. 6(a) but without the slit. In such comparison, the harmonics from electrons following long and short trajectories are both collected. By comparing Figs. 6(a) and 6(b), we note that the MWPs for gas jet at $z = -3$ mm and $z = 0$ mm change significantly, but for $z = 3$ mm, the MWPs in both cases remain rather flat. This shows that a narrow slit in the far field can select the short trajectories effectively.

In Fig. 6(c) we investigate how the MWP depends on the gas pressure for the focusing condition of $z = 3$ mm. The MWP has been normalized by the ratio of the pressure. The three curves would be on top of each other if a complete phase-matching condition had been fulfilled. The curve for higher pressure is slightly lower, indicating that full phase matching is not reached, especially for the lower harmonics. With the increase of pressure, the MWP is much smoother vs energy. In fact, increasing the gas pressure tends to smooth out the harmonics. These results also indicate that the harmonic energy increases quadratically with the gas pressure, which is in agreement with measurements reported in Ref. [67]. In Fig. 6(d) we display the full MWP vs the gas pressure. It shows that the harmonics exhibit better-shaped peaks as the phase-matching condition is favored at higher pressure [59,60].

F. Wavelength scaling of harmonic efficiency

One of the main interests in the study of HHG is to produce bright tabletop xuv or soft x-ray sources, or intense attosecond pulses. Since the single-atom harmonic cutoff energy is proportional to the square of the wavelength of the driving

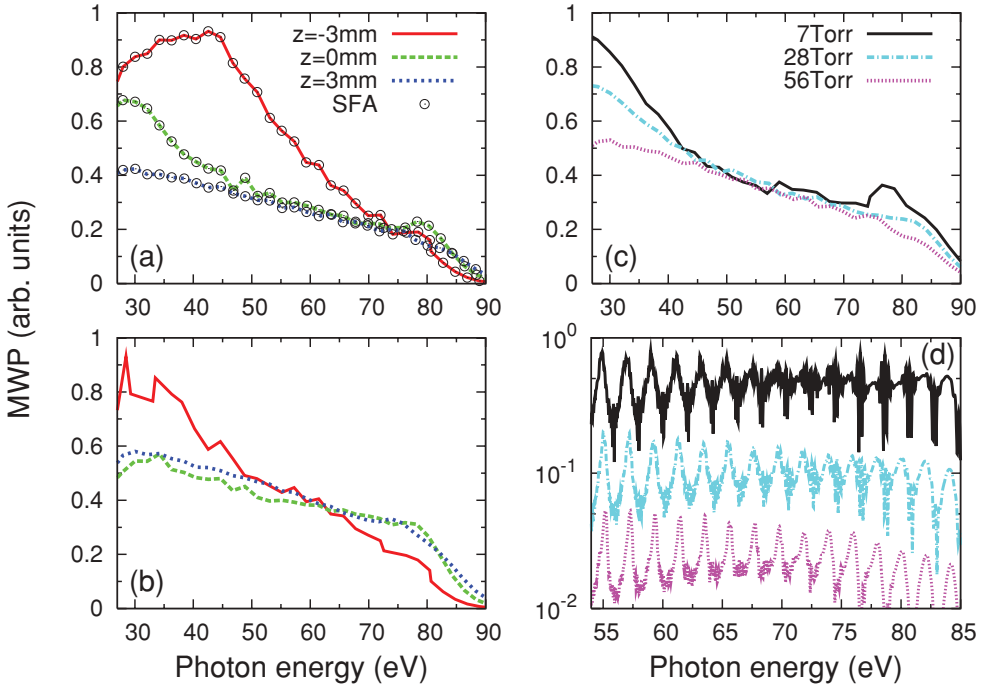

FIG. 6. (Color online) (a) The magnitude (not the intensity) of macroscopic wave packets (MWP) at different gas-jet positions: $z = -3$ mm (before the focus, solid line), $z = 0$ mm (at the focus, dashed line), and $z = 3$ mm (after the focus, dot-dashed line) by QRS. The corresponding ones by SFA are also shown (open circles). The HHG signals are collected at the exit of the slit. (b) Same MWP as in (a), but the total HHG signals are collected without the slit. The curves in (a) and (b) have been normalized separately. (c) Dependence of MWP on gas pressure. Each curve has been normalized by the pressure. (d) The detailed structure of MWP in (c) from 55 to 85 eV. The curves have been shifted for easy visualization.

laser, HHG generated by mid-infrared (MIR) lasers has been of great interest experimentally. While MIR lasers can efficiently reach high-energy photons, the yield is less favorable. It is of interest to study how the HHG yield scales with the laser wavelength. Within the single-atom response level, there have been a few theoretical calculations [68–72]. However, to compare with experimental HHG spectra, macroscopic propagation effect has to be included. A few investigations on the wavelength scaling of HHG experimentally [50,67,73,74] have been reported. However, theoretical analysis is still rather scarce.

To study wavelength scaling of the HHG yields, one has to fix all other parameters that may affect the efficiency of HHG. One also has to decide if it is the total HHG yield or only the HHG yield within a given photon-energy region. In single-atom simulations, the laser parameters can be easily fixed. However, this is not the case in experiments. Theoretical simulations including macroscopic propagation effect are few [75,76]. Since the resulting HHG spectra depend on so many other parameters, as we have demonstrated in the earlier sections, any wavelength scaling laws derived are likely to depend on experimental parameters used. In spite of this limitation, it is still of interest to take a look at the wavelength scaling by using the present QRS model. For this purpose, we define a parameter that describes the efficiency of harmonic generation. This is the ratio between the output energy (total harmonic energy) with respect to the input energy (fundamental laser energy) for different laser wavelengths. According to Ref. [20], the input energy $E_{\rm pulse}$ can be related to the laser duration $\tau_{\rm p}$ and peak intensity I_0 at the focus by $E_{\rm pulse} = \frac{I_0}{2}\pi w_0^2 \tau_{\rm p}$ if the laser beam has a Gaussian distribution in time and space. The output energy can be obtained by integrating the harmonic intensity over a photon-energy region:

$$E_{\rm out} = \int_{\omega_{\rm min}}^{\omega_{\rm max}} \iint |E_{\rm h}(x,y,\omega)|^2 dx dy d\omega. \qquad (32)$$

In Fig. 7(a) we show the single-atom HHG spectra calculated for three wavelengths. Only the envelope of each spectra is shown. In the calculation, the laser intensity and duration are kept as 1.6×10^{14} W/cm^2 and 40 fs, respectively. In Fig. 7(b) the HHG spectra obtained after including macroscopic propagation are shown. In the calculation, the beam waist at the focus is kept as 47.5 μm, a 0.5-mm-long gas jet is placed at 3 mm after the laser focus, and gas pressure is kept at 56 Torr. The yield of each harmonic is obtained by integrating over the whole plane perpendicular to the propagation axis. In Fig. 7(c), the HHG yields are recorded after they have passed a slit (the slit with a width of 100 μm is placed at 24 cm after the gas jet). From Figs. 7(b) and 7(c), we calculate the HHG efficiencies per atom vs the wavelength.

In Fig. 7(a), the ratio of input energy is 1:1:1 for 800-, 1200-, and 1600-nm lasers. If we integrate the HHG yields above 20 eV as the output energy. The resulting energy follows $\lambda^{-3.5\pm0.5}$ shown in Fig. 7(d). Integrating the HHG yields between 20 and 50 eV would give a scaling rule of λ^{-5}. In Tate *et al.* [68], the laser intensity and the number of optical cycles were fixed for 800- and 2000-nm lasers. According to our approach, the ratio

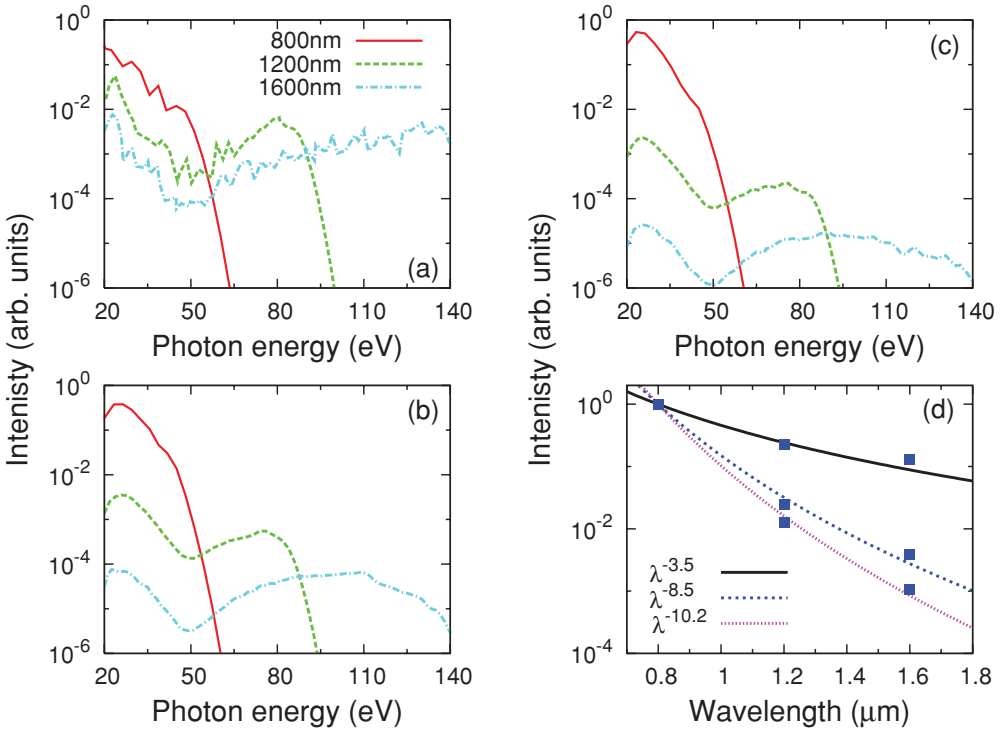

FIG. 7. (Color online) (a) Single-atom HHG spectra and macroscopic HHG spectra without (b) and with (c) the slit for 800-nm (solid lines), 1200-nm (dashed lines), and 1600-nm (dot-dashed lines) lasers. The laser parameters are given in the text. (d) The wavelength dependence of the total integrated HHG yields above 20 eV. The integrated HHG yields in (a), (b), and (c) follow $\lambda^{-3.5\pm0.5}$, $\lambda^{-8.5\pm0.5}$, and $\lambda^{-10.2\pm0.2}$, respectively.

of input energy is 1:2.5 for the 800- and 2000-nm lasers. And their scaling rules at constant intensity of $\lambda^{-(5-6)}$ would be modified as $\lambda^{-(6-7)}$ at a constant input energy.

When propagation effect is considered it is generally known [68,77] that the phase-matching condition is more difficult to meet for longer wavelengths; thus, the HHG efficiency decreases with increasing wavelength. Here we consider the total HHG yields for the lasers used in Fig. 7(b) in which the gas jet is placed at $z = 3$ mm. Since the laser intensity is fixed at the center of the thin gas jet, we calculate that the intensities at the laser focus are 1.78×10^{14} W/cm^2, 2.01×10^{14} W/cm^2, and 2.33×10^{14} W/cm^2, for 800-, 1200-, and 1600-nm lasers, respectively; thus, the input energies have the ratios of 1:1.13:1.31. We find that HHG yields integrated from 20 eV up scale like $\lambda^{-8.5\pm0.5}$, as shown in Fig. 7(d). If we only integrate the harmonics between 20 and 50 eV, then the scaling rule is $\lambda^{-10.5}$.

Experimentally, Colosimo *et al.* [50] reported that the HHG yields between 35 and 50 eV for 2000-nm lasers are about 1000 times smaller than that for 800-nm lasers for experimental conditions that were kept "as fixed as possible." This would give a λ^{-9} dependence in this narrow energy region, which is not too far off from our scaling of $\lambda^{-10.5}$. In addition, Shiner *et al.* [67] reported a scaling rule of $\lambda^{-6.3\pm1.1}$ for the HHG of Xe with a fixed laser intensity. By assuming a perfect phase-matching condition for all the laser wavelengths used, they derived a scaling law of $\lambda^{-6.3\pm1.1}$ that was to be compared to the scaling law derived from the single-atom response. We cannot compare their results with our simulation. They also used a Bessel beam (instead of Gaussian beam) in the experiment and the gas jet was located at the laser focus. Since the HHG yields depend on so many experimental parameters, it is clear that any simple scaling laws derived should be taken with caution. In Fig. 7(d), we also show the scaling law for the case where the HHG yields are collected after the slit. We integrate the HHG signals above 20 eV and obtain the $\lambda^{-10.2\pm0.2}$ scaling. In general, a good phase-matching condition becomes more difficult to meet with increasing laser wavelength. Even if the gas jet is placed after the laser focus, the short trajectories are not selected efficiently for longer wavelength lasers. A slit is usually used to select contributions from short trajectories in the far field. By blocking out contributions [see Fig. 7(c)] from the long trajectories the harmonic efficiency becomes worse.

Based on the above analysis, the HHG yields for long-wave driving lasers under the same experimental conditions appear quite unfavorable. On the other hand, for practical purposes, experimentally high harmonics are to be generated with optimized conditions. In Colosimo *et al.* [50] it was reported that the HHG yields between 35 and 50 eV generated by using 2000-nm lasers can be as high as 50% of that from 800-nm lasers if the experimental conditions were optimized independently. Furthermore, Chen *et al.* [78] demonstrated that it was possible to use much higher pressure to generate HHG for long-wavelength lasers, thus achieving usable photon yields even in the water-window region. Clearly, additional theoretical analysis of macroscopic propagation effects on HHG for long-wavelength driving lasers under different experimental conditions is desirable.

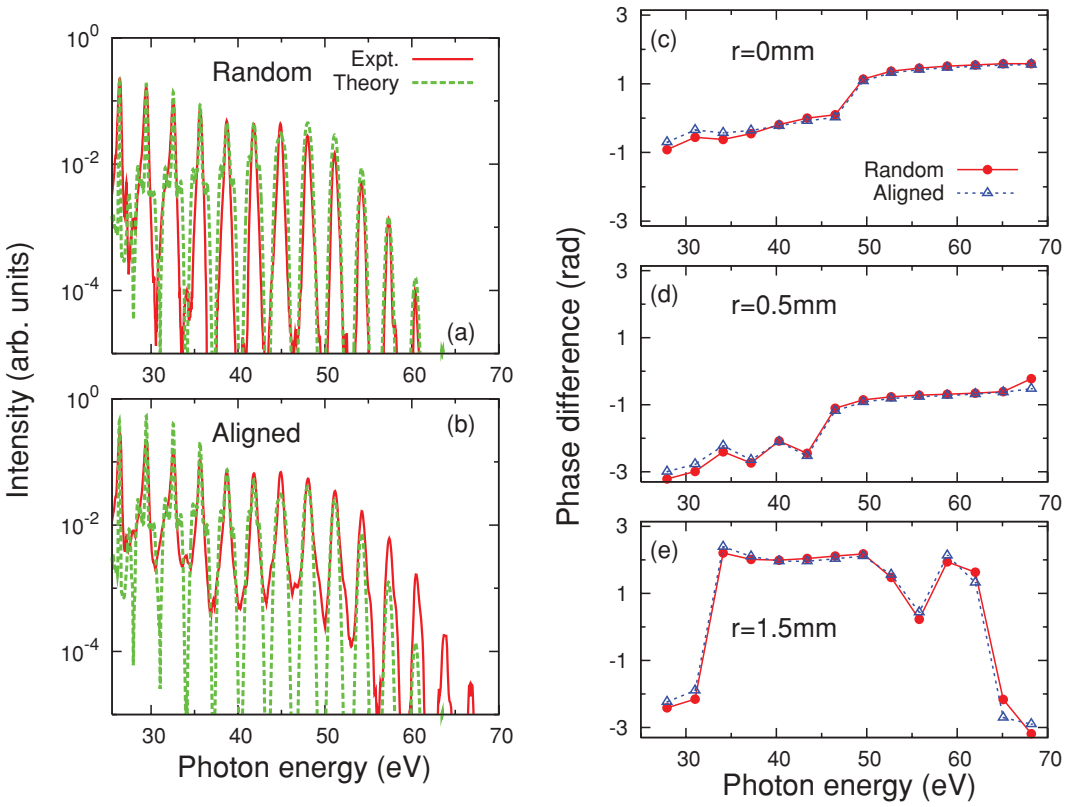

FIG. 8. (Color online) Comparison of theoretical (dashed lines) and experimental (solid lines) HHG yields from (a) random and (b) partially aligned N_2 molecules in an 800-nm laser. Experimental data are from Ref. [79]. Phase difference between consecutive harmonics of random (solid circles) and partially aligned (open triangles) N_2 molecules in the far field at different radial distances: (c) $r = 0$ mm, (d) $r = 0.5$ mm, and (e) $r = 1.5$ mm.

G. Macroscopic HHG spectra of N_2 in an 800-nm laser

The QRS has been used to calculate HHG spectra from single molecules. In order to compare with experimental data, it is often assumed that HHG measured in the experiment is taken under the perfect phase-matching conditions. While such a model has been shown to be successful in interpreting a number of experimental observations [17,43,44], it is still crucial to understand the effect of propagation on the HHG in the medium. In Figs. 8(a) and 8(b) we show the macroscopic HHG spectra generated by N_2 molecules that are isotropically distributed or partially aligned along the polarization axis of an 800-nm laser. The HHG spectra have been reported recently [79] using 800- and 1200-nm lasers, and the results from 1200-nm laser have been recently analyzed [46]. To achieve good agreement with experiment in the cutoff region, we need to use peak intensity of 1.8×10^{14} W/cm^2 instead of 2.3×10^{14} W/cm^2 in the experiment. We use the other parameters as close as those given in the experiment: pulse duration is $\sim$32 fs, beam waist at the focus is $\sim$40 μm, and a slit with a width of 100 μm is placed at 24 cm after the gas jet. A 1-mm-wide gas jet is located 3 mm after the laser focus. Using the QRS, we first obtain induced dipoles for fixed-in-space molecules for different laser intensities. They are then averaged coherently according to the alignment distribution of molecules by Eq. (25). The resulting induced dipoles are then fed into Eq. (17). In the experiment, the degree of alignment was estimated to be $\langle \cos^2 \theta \rangle = 0.6$–$0.65$; we use an alignment distribution of $\cos^4 \theta$ in the simulation. Note that only the highest occupied molecular orbital (HOMO) is included in the calculation. This is adequate since contributions from HOMO-1 is important only for molecules that are nearly perpendicular to the polarization axis [44,80].

Figures 8(a) and 8(b) show the good overall agreement between experiment and theory for both randomly distributed and partially aligned N_2. The experimental spectra reveal a weak minimum at 39 ± 2 eV [79] for both aligned and unaligned molecules. The theory also predicts a minimum near 45 eV, and the position of minimum is not shifted from random to the partially aligned N_2. For aligned N_2, we note that McFarland *et al.* [81] reported a weak minimum around 39 eV in the HHG spectra using an 800-nm laser. However, the minimum was observed at about 45 eV in Torres *et al.* [82] using an 800-nm laser and at about 38 eV using a 1300-nm laser for unaligned N_2 (see their Fig. 3). For 1200-nm lasers, minimums in HHG spectra from the experiment [79] and the simulation [46] have also been reported. The exact location of the minimum is not always identical since it can be somewhat altered due to the energy dependence of the MWP [see Fig. 9(a)], which changes with laser parameters and experimental conditions. Despite of the difference in the positions of the minima between the simulation and experiment, we consider that the overall agreement in the two spectra is quite satisfactory. Note that the agreement between theory and experiment is better in Fig. 8(a) than

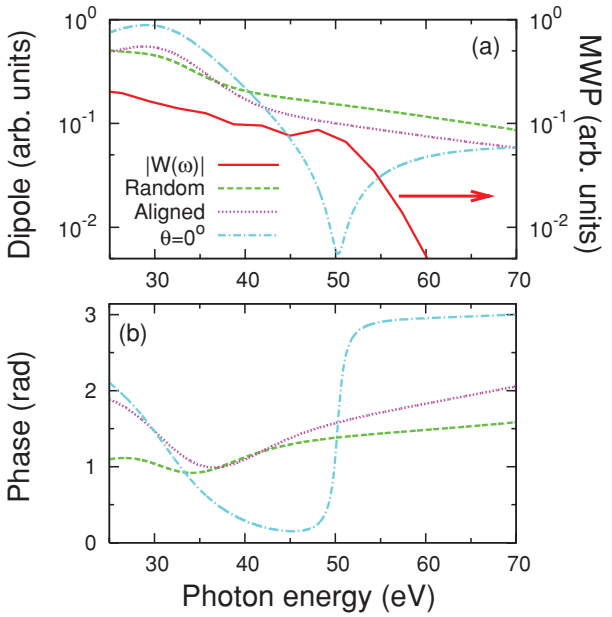

FIG. 9. (Color online) (a) Macroscopic wave packet (MWP) for an 800-nm laser (solid line), and averaged photoionization (PI) transition dipole moments (parallel component) for randomly distributed (dashed line), partially aligned (dotted line), and perfectly aligned ($\theta = 0^\circ$, dot-dashed line) N_2 molecules. (b) The photon-energy dependence of the phase for averaged PI transition dipoles in (a).

that in Fig. 8(b). Since there are still some uncertainties in determining the alignment distribution exactly at the rotational half revival (maximal alignment), we expect to improve the agreement between theory and experiment in Fig. 8(b) with more precise alignment distribution of $\rho(\theta)$ in Eq. (25). In the future, it is desirable to compare the HHG spectra taken at different alignment angles together, which will help to clarify the discrepancies between theory and experiment.

In Figs. 8(c)–8(e) we show the phase difference between neighboring harmonics for randomly distributed and partially aligned N_2 molecules in the far field for different radial positions from the propagation axis. As mentioned in Sec. III D, phase differences, which reveal emission times of harmonics [83] and can be measured by reconstruction of attosecond beating by interference of two-photon transition [84,85] technique, are significant for the generation of attosecond pulses [86]. Near the axis, we note that the phase difference is linearly changed vs photon energy in the plateau ending up by a sharp rise near about 48 eV in Fig. 8(c) and 45 eV in Fig. 8(d), and beyond the cutoff it is almost a constant. The nearly constant phase difference was observed by Mairesse *et al.* [87] for atomic targets to optimize the conditions for attosecond pulse generation. Since the phase changes rapidly near the minimum of the harmonic spectra, this explains that the position of the HHG minimum in the integrated spectra can be easily changed, depending on how the integrated spectra are measured. We comment that the phase difference vs photon energy in Fig. 8(e) is less regular. These harmonics, taken at a position away from the axis, have large contributions from long trajectories and they are not suitable for attosecond pulse generation. Finally, phase difference for randomly distributed and partially aligned N_2 agree well. The small variation comes from the slightly different derivative of the phase of averaged transition dipoles for random and partially aligned N_2 [see Fig. 9(b)].

To understand the results shown in Fig. 8, we show the MWP for the laser used and PI transition dipole moment (parallel component only) for N_2 molecules fixed in space, as well as the averaged PI transition dipoles defined by Eq. (28) for randomly distributed and partially aligned N_2 molecules in Fig. 9. According to Eq. (27), macroscopic HHG yields can be expressed as the product of a MWP and an averaged transition dipole. The MWP (magnitude) is identical for random or partially aligned N_2 under the same laser and experimental condition. The transition dipole for fixed-in-space molecules shows a minimum at photon energy that depends on the angle between the molecular axis and the laser polarization axis (see Refs. [17,45]). An average over the angular distribution of the molecules washes out the minimum, except for a relatively faster drop of the transition dipole near 35–45 eV. The effect of angular average also washes out the rapid phase change in the transition dipole moment. For molecules fixed at $\theta = 0^\circ$, Fig. 9(b) shows a rapid phase change of near π in a very narrow energy region near 50 eV, that is, at the position of the minimum in Fig. 9(a). However, after the angular average, one can only see somewhat faster phase change at small photon energies. Since both the MWP and the transition dipole exhibit minor energy dependence, the actual minimum position of the HHG is difficult to locate accurately. With much better aligned molecules, the position of the minimum can probably be better determined. According to Eqs. (27) and (28), the averaged PI transition dipole can be obtained from the experimental HHG spectra, and it could be used to retrieve the alignment-dependent ionization probability, $N(\theta)$. This may provide another method to check the calculated $N(\theta)$ [42].

IV. SUMMARY AND OUTLOOK

In this paper we have described a complete theory for HHG in a macroscopic atomic or molecular medium. Our approach is based on the simultaneous solution of the coupled Maxwell's equations describing macroscopic propagation of both driving laser pulse and its high harmonic fields together with the microscopic induced dipoles. For the latter we use the recently developed QRS theory for a single-atom or -molecule response. This scheme provides a simple and efficient method for calculating HHG from a macroscopic medium, which is otherwise formidable, especially in the case of molecular targets.

Our results show quantitative good agreements with recent experimental HHG measurements [46,79] for either Ar or N_2 targets. For different laser and experimental conditions, we present the detailed analysis of HHG intensity and phase. Since the calculation which includes macroscopic propagation for an isotropic or an aligned molecular target is quite scarce [46], we hope that this paper will further stimulate the interest in establishing quantitative theory for HHG, which can compare directly with real experiments for partially aligned media. We note that in this paper the effect of absorption and dispersion of high harmonics are neglected for molecular N_2,

which should be adequate at low gas pressure. In general, absorption and dispersion are anisotropic in case of aligned molecules, which are not available generally in the literature. One of the most important results of this paper is that at the macroscopic level under typical experimental conditions HHG spectra can be factorized as a product of a MWP and a PR transition dipole. The latter is a property of the target only. This factorization provides a solid foundation for extracting the molecular structures from HHG spectra. As demonstrated recently [7], HHG has been used for ultrafast probes of excited molecules, our work also provides the needed theoretical basis for that.

ACKNOWLEDGMENTS

This work was supported in part by Chemical Sciences, Geosciences and Biosciences Division, Office of Basic Energy Sciences, Office of Science, US Department of Energy.

[1] A. Rundquist, C. G. Durfee III , Z. Chang, C. Herne, S. Backus, M. M. Murnane, and H. C. Kapteyn, Science **280**, 1412 (1998).
[2] R. A. Bartels, A. Paul, H. Green, H. C. Kapteyn, M. M. Murnane, S. Backus, I. P. Christov, Y. Liu, D. Attwood, and C. Jacobsen, Science **297**, 376 (2002).
[3] F. Krausz and M. Ivanov, Rev. Mod. Phys. **81**, 163 (2009).
[4] P. Agostini and L. F. DiMauro, Rep. Prog. Phys. **67**, 813 (2004).
[5] J. Itatani, J. Levesque, D. Zeidler, H. Niikura, H. Pépin, J. C. Kieffer, P. B. Corkum, and D. M. Villeneuve, Nature (London) **432**, 867 (2004).
[6] O. Smirnova, Y. Mairesse, S. Patchkovskii, N. Dudovich, D. Villeneuve, P. Corkum, and M. Yu. Ivanov, Nature (London) **460**, 972 (2009).
[7] H. J. Wörner, J. B. Bertrand, D. V. Kartashov, P. B. Corkum, and D. M. Villeneuve, Nature (London) **466**, 604 (2010).
[8] V. H. Le, A. T. Le, R. H. Xie, and C. D. Lin, Phys. Rev. A **76**, 013414 (2007).
[9] J. L. Krause, K. J. Schafer, and K. C. Kulander, Phys. Rev. Lett. **68**, 3535 (1992).
[10] P. B. Corkum, Phys. Rev. Lett. **71**, 1994 (1993).
[11] M. B. Gaarde, M. Murakami, and R. Kienberger, Phys. Rev. A **74**, 053401 (2006).
[12] M. Lewenstein, Ph. Balcou, M. Yu. Ivanov, A. L'Huillier, and P. B. Corkum, Phys. Rev. A **49**, 2117 (1994).
[13] M. B. Gaarde and K. J. Schafer, Phys. Rev. A **65**, 031406 (2002).
[14] M. B. Gaarde, J. L. Tate, and K. J. Schafer, J. Phys. B **41**, 132001 (2008).
[15] C. D. Lin, A. T. Le, Z. Chen, T. Morishita, and R. R. Lucchese, J. Phys. B **43**, 122001 (2010).
[16] T. Morishita, A. T. Le, Z. Chen, and C. D. Lin, Phys. Rev. Lett. **100**, 013903 (2008).
[17] A. T. Le, R. R. Lucchese, S. Tonzani, T. Morishita, and C. D. Lin, Phys. Rev. A **80**, 013401 (2009).
[18] C. Jin, A. T. Le, and C. D. Lin, Phys. Rev. A **79**, 053413 (2009).
[19] E. Esarey, P. Sprangle, J. Krall, and A. Ting, IEEE J. Quantum Electron. **33**, 1879 (1997).
[20] E. Takahashi, V. Tosa, Y. Nabekawa, and K. Midorikawa, Phys. Rev. A **68**, 023808 (2003).
[21] M. Geissler, G. Tempea, A. Scrinzi, M. Schnürer, F. Krausz, and T. Brabec, Phys. Rev. Lett. **83**, 2930 (1999).
[22] S. C. Rae and K. Burnett, Phys. Rev. A **46**, 1084 (1992).
[23] E. Priori *et al.*, Phys. Rev. A **61**, 063801 (2000).
[24] M. V. Ammosov, N. B. Delone, and V. P. Krainov, Zh. Eksp. Teor. Fiz. **91**, 2008 (1986) [Sov. Phys. JETP **64**, 1191 (1986)].
[25] X. M. Tong, Z. X. Zhao, and C. D. Lin, Phys. Rev. A **66**, 033402 (2002).
[26] X. M. Tong and C. D. Lin, J. Phys. B **38**, 2593 (2005).
[27] A. Börzsönyi, Z. Heiner, M. P. Kalashnikov, A. P. Kovács, and K. Osvay, Appl. Opt. **47**, 4856 (2008).
[28] P. J. Leonard, At. Data Nucl. Data Tables **14**, 21 (1974).
[29] H. J. Lehmeier, W. Leupacher, and A. Penzkofer, Opt. Commun. **56**, 67 (1985).
[30] X. F. Li, A. L'Huillier, M. Ferray, L. A. Lompré, and G. Mainfray, Phys. Rev. A **39**, 5751 (1989).
[31] J. K. Koga, N. Naumova, M. Kando, L. N. Tsintsadze, K. Nakajima, S. V. Bulanov, H. Dewa, H. Kotaki, and T. Tajima, Phys. Plasmas **7**, 5223 (2000).
[32] R. W. Boyd, *Nonlinear Optics*, 2nd ed. (Academic Press, San Diego, 2003).
[33] V. Tosa, H. T. Kim, I. J. Kim, and C. H. Nam, Phys. Rev. A **71**, 063807 (2005).
[34] C. T. Chantler, K. Olsen, R. A. Dragoset, J. Chang, A. R. Kishore, S. A. Kotochigova, and D. S. Zucker, *X-ray Form Factor, Attenuation and Scattering Tables* (version 2.1) (National Institute of Standards and Technology, Gaithersburg, MD, 2005) [http://physics.nist.gov/ffast].
[35] B. L. Henke, E. M. Gullikson, and J. C. Davis, At. Data Nucl. Data Tables **54**, 181 (1993).
[36] A. E. Siegman, *Lasers* (University Science, Mill Valley, CA, 1986).
[37] A. L'Huillier, Ph. Balcou, S. Candel, K. J. Schafer, and K. C. Kulander, Phys. Rev. A **46**, 2778 (1992).
[38] V. Tosa, K. T. Kim, and C. H. Nam, Phys. Rev. A **79**, 043828 (2009).
[39] A. T. Le, T. Morishita, and C. D. Lin, Phys. Rev. A **78**, 023814 (2008).
[40] H. G. Muller, Phys. Rev. A **60**, 1341 (1999).
[41] R. R. Lucchese, G. Raseev, and V. McKoy, Phys. Rev. A **25**, 2572 (1982).
[42] S. F. Zhao, C. Jin, A. T. Le, T. F. Jiang, and C. D. Lin, Phys. Rev. A **81**, 033423 (2010).
[43] A. T. Le, R. R. Lucchese, M. T. Lee, and C. D. Lin, Phys. Rev. Lett. **102**, 203001 (2009).
[44] A. T. Le, R. R. Lucchese, and C. D. Lin, J. Phys. B **42**, 211001 (2009).
[45] C. Jin, A. T. Le, S. F. Zhao, R. R. Lucchese, and C. D. Lin, Phys. Rev. A **81**, 033421 (2010).
[46] C. Jin, H. J. Wörner, V. Tosa, A. T. Le, J. B. Bertrand, R. R. Lucchese, P. B. Corkum, D. M. Villeneuve, and C. D. Lin, e-print arXiv:1012.1892.
[47] J. W. Cooper, Phys. Rev. **128**, 681 (1962).
[48] H. J. Wörner, H. Niikura, J. B. Bertrand, P. B. Corkum, and D. M. Villeneuve, Phys. Rev. Lett. **102**, 103901 (2009).
[49] S. Minemoto, T. Umegaki, Y. Oguchi, T. Morishita, A. T. Le, S. Watanabe, and H. Sakai, Phys. Rev. A **78**, 061402 (2008).

[50] P. Colosimo *et al.*, Nat. Phys. **4**, 386 (2008).
[51] J. P. Farrell, L. S. Spector, B. K. McFarland, P. H. Bucksbaum, M. Gühr, M. B. Gaarde, and K. J. Schafer, e-print arXiv:1011.1297.
[52] K. Varjú *et al.*, J. Mod. Opt. **52**, 379 (2005).
[53] A. Zaïr *et al.*, Phys. Rev. Lett. **100**, 143902 (2008).
[54] X. He *et al.*, Phys. Rev. A **79**, 063829 (2009).
[55] E. Benedetti, J.-P. Caumes, G. Sansone, S. Stagira, C. Vozzi, and M. Nisoli, Opt. Express **14**, 2242 (2006).
[56] J. Norin *et al.*, Phys. Rev. Lett. **88**, 193901 (2002).
[57] T. Sekikawa, T. Katsura, S. Miura, and S. Watanabe, Phys. Rev. Lett. **88**, 193902 (2002).
[58] M. B. Gaarde, F. Salin, E. Constant, Ph. Balcou, K. J. Schafer, K. C. Kulander, and A. L'Huillier, Phys. Rev. A **59**, 1367 (1999).
[59] T. Popmintchev, M.-C. Chen, A. Bahabad, M. Gerrity, P. Sidorenko, O. Cohen, I. P. Christov, M. M. Murnane, and H. C. Kapteyn, Proc. Natl. Acad. Sci. USA **106**, 10516 (2009).
[60] C. Winterfeldt, C. Spielmann, and G. Gerber, Rev. Mod. Phys. **80**, 117 (2008).
[61] G. Doumy, J. Wheeler, C. Roedig, R. Chirla, P. Agostini, and L. F. DiMauro, Phys. Rev. Lett. **102**, 093002 (2009).
[62] P. Salières, T. Ditmire, M. D. Perry, A. L'Huillier, and M. Lewenstein, J. Phys. B **29**, 4771 (1996).
[63] P. Salières, A. L'Huillier, Ph. Antoine, and M. Lewenstein, Adv. At. Mol. Opt. Phys. **41**, 83 (1999).
[64] R. López-Martens *et al.*, Phys. Rev. Lett. **94**, 033001 (2005).
[65] P. Antoine, A. L'Huillier, and M. Lewenstein, Phys. Rev. Lett. **77**, 1234 (1996).
[66] P. Salières, Ph. Antoine, A. de Bohan, and M. Lewenstein, Phys. Rev. Lett. **81**, 5544 (1998).
[67] A. D. Shiner, C. Trallero-Herrero, N. Kajumba, H.-C. Bandulet, D. Comtois, F. Légaré, M. Giguère, J.-C. Kieffer, P. B. Corkum, and D. M. Villeneuve, Phys. Rev. Lett. **103**, 073902 (2009).
[68] J. Tate, T. Auguste, H. G. Muller, P. Salières, P. Agostini, and L. F. DiMauro, Phys. Rev. Lett. **98**, 013901 (2007).
[69] K. Schiessl, K. L. Ishikawa, E. Persson, and J. Burgdörfer, Phys. Rev. Lett. **99**, 253903 (2007).
[70] M. V. Frolov, N. L. Manakov, and A. F. Starace, Phys. Rev. Lett. **100**, 173001 (2008).
[71] A. Gordon and F. X. Kärtner, Opt. Express **13**, 2941 (2005).
[72] P. Lan, E. J. Takahashi, and K. Midorikawa, Phys. Rev. A **81**, 061802 (2010).
[73] T. Popmintchev, M.-C. Chen, O. Cohen, M. E. Grisham, J. J. Rocca, M. M. Murnane, and H. C. Kapteyn, Opt. Lett. **33**, 2128 (2008).
[74] E. L. Falcão-Filho, C.-J. Lai, K.-H. Hong, V.-M. Gkortsas, S.-W. Huang, L.-J. Chen, and F. X. Kätner, Appl. Phys. Lett. **97**, 061107 (2010).
[75] V. S. Yakovlev, M. Ivanov, and F. Krausz, Opt. Express **15**, 15351 (2007).
[76] E. L. Falcão-Filho, V. M. Gkortsas, A. Gordon, and F. X. Kätner, Opt. Express **17**, 11217 (2009).
[77] B. Shan and Z. Chang, Phys. Rev. A **65**, 011804 (2001).
[78] M.-C. Chen, P. Arpin, T. Popmintchev, M. Gerrity, B. Zhang, M. Seaberg, D. Popmintchev, M. M. Murnane, and H. C. Kapteyn, Phys. Rev. Lett. **105**, 173901 (2010).
[79] H. J. Wörner, J. B. Bertrand, P. Hockett, P. B. Corkum, and D. M. Villeneuve, Phys. Rev. Lett. **104**, 233904 (2010).
[80] B. K. McFarland, J. P. Farrell, P. H. Bucksbaum, and M. Gühr, Science **322**, 1232 (2008).
[81] B. K. McFarland, J. P. Farrell, P. H. Bucksbaum, and M. Gühr, Phys. Rev. A **80**, 033412 (2009).
[82] R. Torres *et al.*, Opt. Express **18**, 3174 (2010).
[83] Y. Mairesse *et al.*, Science **302**, 1540 (2003).
[84] P. M. Paul, E. S. Toma, P. Breger, G. Mullot, F. Augé, Ph. Balcou, H. G. Muller, and P. Agostini, Science **292**, 1689 (2001).
[85] W. Boutu *et al.*, Nat. Phys. **4**, 545 (2008).
[86] H. Wabnitz *et al.*, Eur. Phys. J. D **40**, 305 (2006).
[87] Y. Mairesse *et al.*, Phys. Rev. Lett. **93**, 163901 (2004).